Low temperature carbon dioxide gas sensor based on yolk-shell ceria nanospheres

Cecilia A. Zito,[1,2] Tarcísio M. Perfecto,[1] Ann-Christin Dippel,[3] Diogo P. Volanti,[1]* and Dorota Koziej[2]*

1 Laboratory of Materials for Sustainability (LabMatSus), São Paulo State University (UNESP), Rua Cristóvão Colombo 2265, 15054000 São José do Rio Preto, Brazil

2 Center for Hybrid Nanostructures (CHyN), Institute of Nanostructure and Solid State Physics, University of Hamburg, Luruper Chaussee 149, 22607 Hamburg, Germany

3 Deutsches Elektronen-Synchrotron DESY, Notkestrasse 85, 22607 Hamburg, Germany

Corresponding authors:

*Dorota Koziej. E-mail: dorota.koziej@uni-hamburg.de

*Diogo P. Volanti. E-mail: diogo.volanti@unesp.br

Abstract

Monitoring carbon dioxide (CO_2) levels is extremely important in a wide range of applications. Although metal oxide-based chemoresistive sensors have emerged as a promising approach for CO_2 detection, the development of efficient CO_2 sensors at low temperature remains a challenge. Herein, we report a low temperature hollow nanostructured CeO_2-based sensor for CO_2 detection. We monitor the changes in the electrical resistance after CO_2 pulses in a relative humidity of 70% and show the high performance of the sensor at 100°C. The yolk-shell nanospheres have not only two times higher sensitivity but also significantly increased stability and reversibility, faster response times, and greater CO_2 adsorption capacity than commercial ceria nanoparticles. The improvements in the CO_2 sensing performance are attributed to hollow and porous structure of the yolk-shell nanoparticles allowing for enhanced gas diffusion and high specific surface area. We present an easy strategy to enhance the electrical and sensing properties of metal oxides at a low operating temperature that is desirable for practical applications of CO_2 sensors.

Keywords: CO_2 sensing, chemoresistive, ceria, hollow structure, PDF analysis

1. Introduction

The concentration of polluting, toxic, and harmful gases in the atmosphere has increased in the last years due to human activities, which has huge impact on the environment. Carbon dioxide (CO_2) emissions, in particular, have huge impact on global warming and climate change because CO_2 is the main greenhouse gas, and its concentration has been drastically increasing since pre-industrial times.[1] CO_2 also presents toxicity in humans for being an asphyxiant and inhalation toxicant,[2] which causes numerous deaths in confined spaces, according to the Occupational Safety and Health Administration (OSHA).[3] Hence, much effort has been directed to develop CO_2 sensors to monitor air quality and improve human well-being in indoor and outdoor environments. The levels of CO_2 are commonly measured using sensors based on spectroscopic techniques, such as non-dispersive infrared (NDIR),[4] and electrochemical methods.[5,6] However, these kinds of sensors have some drawbacks, including high costs, power consumption, complex operation conditions, and limitation of miniaturization.[7,8]

An alternative approach to detect CO_2 is the use of chemoresistive sensors due to their low cost, easy to use, simplicity in operation, small size, and reliability.[9] In this sense, there has been an increased number of researches on CO_2 sensors composed of pure metal oxides and their composites, including $La_2O_2CO_3$,[10] NdO_2CO_3,[11] CuO,[12] ZnO,[13] SnO_2,[9] $CuO/CuFe_2O_4$,[14] Ag@CuO/ZnO,[15] $Ag@CuO/BaTiO_3$.[16] Yet, most of these sensing materials present low sensitivity toward CO_2 given the CO_2 inertia regarding reduction or oxidation reactions,[12,17] or the sensors require elevated temperature usually above 200 °C to achieve the best operating conditions.[9,12,13,15,18] The inorganic-organic composites provide viable alternative to sense CO_2 at low temperature, however they are suffering from very slow recovery time.[19–21] Thus, it is necessary to explore strategies to improve the working temperature and recovery time of sensors.

The design of metal oxide-based sensors in a suitable morphology can significantly improve their gas-sensing performance. Thus, hollow nanostructured materials have attracted much attention as gas sensors due to their potential for sensitivity, response and recovery times, and stability of sensors for CO,[22] H_2S,[23] H_2,[24] ethanol,[25] and triethylamine.[26] Hollow structures differ from bulk materials in terms of increased specific surface area, porous shells, permeability to gas adsorption, gases access from inside and outside, effective and fast gas-diffusion.[22,27,28] Albeit the reports cited beforehand, few studies have been carried out to study

the effects of hollow nanostructured materials on the CO_2 sensing performance of metal oxides.

Herein, we demonstrate that designing hollow and porous materials can be an efficient strategy to improve the CO_2 sensing properties of metal oxides. To this end, we explore the synthesis of yolk-shell CeO_2 nanospheres *via* a simple microwave-assisted solvothermal method and their subsequent application as a CO_2 sensor under humid conditions. The CO_2 sensing tests reveal the highest sensitivity at the low temperature of 100 °C in 70% relative humidity (RH). The yolk-shell CeO_2 nanospheres-based sensors exhibit two times higher sensor signal and more than 10 faster response and recovery time than the sensor based on commercial CeO_2 nanoparticles at the same operating conditions. Our experiments suggest that unlike for CeO_2 used for catalysis at elevated temperatures, the improvement of sensing performance at 100°C is purely due to the unique morphology and not to surface reduction and oxidation of ceria.

2. Experimental Section

2.1. Materials

$Ce(NO_3)_3.6H_2O$ (>99% trace metals basis), urea (99.0–100.5% purity), citric acid monohydrate (≥ 98% purity), ethylene glycol (≥ 99% purity), and CeO_2 powder (< 5 μm, 99.9% trace metals basis) were supplied by Sigma-Aldrich and H_2O_2 (30%) by Vetec. The chemicals were used as received without further purification.

2.2. Synthesis of yolk-shell CeO_2

To fabricate the yolk-shell CeO_2 nanospheres, we adapted a formerly reported method.[29] In a typical synthesis, of $Ce(NO_3)_3 \cdot 6H_2O$ (282.67 mg, 0.651 mmol), urea (40.18 mg, 0.669 mmol) and citric acid monohydrate (68.59 mg, 0.326 mmol) were dissolved in a mixture 56 mL of Milli-Q ultrapure water with a resistivity of 18.2 MΩ·cm at 25 °C and 8 mL of ethylene glycol, and stirred for 20 min. Then, H_2O_2 (400 μL) was added, and the mixture was stirred for 5 min. The mixture was then transferred to a 100 mL Teflon container, sealed in a Teflon® autoclave with a stainless-steel seal and placed in a microwave-system[30] (2.45 GHz/800 W) for 90 min at 160 °C. After cooling, the precipitate was centrifuged, washed with deionized water (5x), ethanol (1x), and dried in an oven at 85 °C. The schematic illustration for the synthesis of yolk-shell CeO_2 nanospheres is shown in Figure 1.

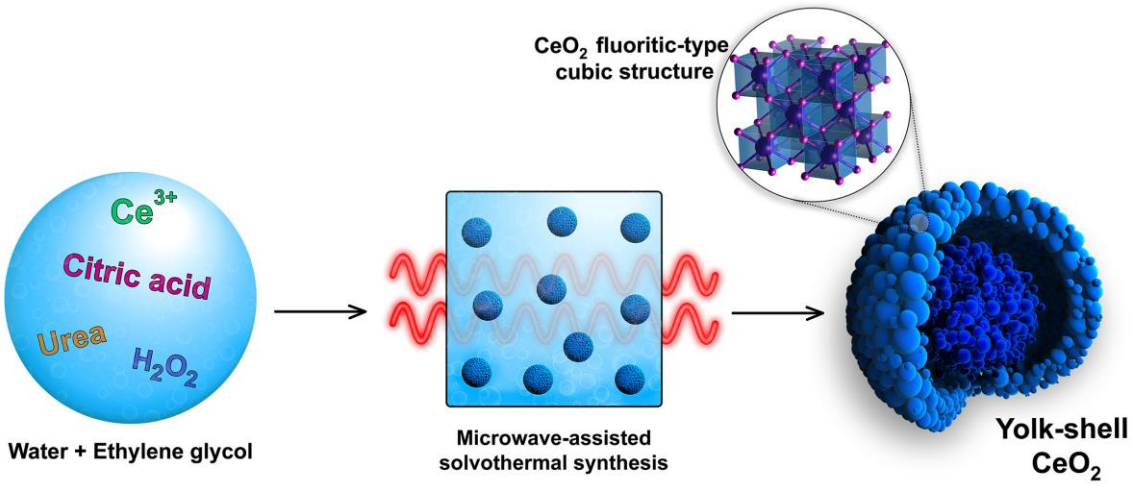

Figure 1. Schematic illustration of the microwave-assisted solvothermal synthesis of the yolk-shell CeO_2 nanospheres.

2.3. Experimental methods

Powder X-ray diffraction (PXRD) patterns were measured on a Rigaku MiniFlex 300 powder diffractometer using Cu Kα radiation (λ=1.5418 Å), operated at 30 kV and 10 mA. Transmission electron microscopy (TEM) and high-resolution TEM (HRTEM) images were taken on JEOL JEM 2100 microscope operated at 200 kV of acceleration voltage. Field-emission scanning electron microscopy (FESEM) and energy-dispersive X-ray spectroscopy (EDS) were conducted on a JEOL JSM-7500F microscope operated at 2 and 10 kV for the respective analyses. Attenuated total reflection Fourier transform infrared (ATR-FTIR) spectroscopy was performed on a PerkinElmer Spectrum Two™ spectrometer. Raman spectrum was recorded using a HORIBA T64000 triple grating spectrometer with a laser excitation of 633 nm. X-ray photoelectron spectroscopy (XPS) was carried out on a Thermo Scientific K-Alpha Spectrometer using Al Kα X-ray source (1486.6 keV). The binding energies were calibrated taking the C 1s peak at 284.8 eV. N_2 adsorption isotherms were measured at 77 K using a Micromeritics' Gemini® VII 2390 surface area analyzer. The specific surface areas were determined by the Brunauer-Emmet-Teller (BET) method.

Total X-ray scattering measurements were carried out at beamline P07 at PETRA III at Deutsches Elektronen-Synchrotron DESY, Hamburg, Germany. A Kapton capillary with inner diameter 1.024 mm was filled with the powder, placed inside a chamber filled with He and then measured at a photon energy of 98.2 keV (λ = 0.1263 Å). The 2D diffraction patterns were collected using a PerkinElmer XRD1621 detector (2048 x 2048 pixels) with an exposure time of 1 s and 60 summed exposures. The pyFAI software[31] was used for calibration of sample to detector distance, beam center and non-orthogonality of the incident beam and the detector plane using a LaB_6 standard, and for the azimuthal integration of the 2D diffraction

patterns. The pair distribution function (PDF) was obtained from the integrated pattern using the PDFgetX3 software.[32] Before the Fourier transform, the integrated data were corrected for background by subtracting the scattering data of an empty Kapton capillary measured at the same conditions. The Q_{max} parameter, *i.e.*, the finite data range used in the Fourier transform step,[33] was set to 18.1 $Å^{-1}$. The obtained PDF was refined applying PDFgui,[33] and Q_{broad} and Q_{damp} were determined as 0.016 and 0.025 $Å^{-1}$, respectively, from calibration with LaB_6.

2.4. Sensor fabrication

The powder of yolk-shell CeO_2 nanospheres was mixed with ethylene glycol using a pestle and mortar to form a paste, which was deposited into alumina substrate containing interdigitated Pt electrodes on the front side for the resistance measurements, and a Pt heater on the backside. The substrate containing the film was annealed at 400 °C for 1 h at a heating rate of 10 °C min^{-1} to remove the ethylene glycol and stabilize the sensing layer. The same method was employed to prepare the reference sensor based on commercial CeO_2 nanoparticles.

2.5. Gas-sensing performance

The CO_2 sensing tests were conducted with sensors placed in a continuous-flow Teflon® chamber. The temperature of the measurement was adjusted using a DC power supply. A gas-mixing system was used to adjust the CO_2 concentrations and the relative humidity (RH) at a constant flow of 200 mL min^{-1} in synthetic air. Before the first CO_2 pulse, the sensors were conditioned in humid air flow for several hours until a stable baseline was achieved. To monitor the variations of the resistance of the sensors during the exposure to CO_2 pulses, a programmable electrometer (Keithley model 617) was used. The sensor signal was defined by the ratio R_{CO2}/R_0, where R_{CO2} is the resistance measured at the end of the gas exposure and R_0 is the resistance in synthetic air without the target gas. The response and recovery times are defined, respectively, as the time to reach 90% of the maximum resistance change after the CO_2 exposure and to recovery 90% of the initial baseline resistance after the CO_2 pulse.

2.6. CO_2 adsorption measurement

The CO_2 adsorption properties of the materials were assessed by thermogravimetric[34,35] (TG) analysis in a Perkin-Elmer TGA-4000 thermogravimetric analyzer. Before the adsorption measurements, ~10–15 mg of the sample was heated at 400 °C (the temperature of the sensor preparation) in 20 mL min^{-1} N_2 flow until obtaining a stable weight and then cooled down to 100 °C. The temperature of 100 °C was maintained constant

in an N_2 flow for 10 minutes; then the flow was changed to 100 mL min^{-1} of pure CO_2 for 5 minutes. The capacity of CO_2 adsorption was determined by the weight gain of the sample after the CO_2 exposure.

3. Results and discussion

We investigate the morphology and particle size of the sample with FESEM and TEM, as shown in Figure 2. The sample is composed of nanoparticles agglomerated in a spherical shape as shown in Figure 2a. The TEM images in Figure 2b,c and Figure S1a reveal that the nanospheres are yolk-shell structured, which have an inner core and a porous outer shell with a hollow space between them, and each nanosphere is composed of small nanoparticles. We measure the diameter of the CeO_2 nanospheres in a series of TEM images and obtain the size distribution shown in Figure S1b, resulting in an average nanosphere diameter of 190 ± 20 nm. The diffraction rings in the selected area electron diffraction (SAED), shown in Figure 2d, are typical of polycrystalline materials, and the broad rings indicate the nanosized sample. The SAED pattern can be indexed to the cubic fluorite-type CeO_2. Moreover, the nanoparticles are highly crystalline, and their size is about 5 nm as shown in HRTEM Figures 2e-f. The lattice fringes with a *d*-spacing of 0.31 nm correspond to the (111) lattice plane of cubic CeO_2. The phase purity of the sample is confirmed by PXRD analysis as shown in Supporting Information, Figure S2. The complementary characterizations of the composition and surface species by means of EDS, ATR-FTIR, Raman, and XPS are presented in Supporting Information, Figure S3-S6.

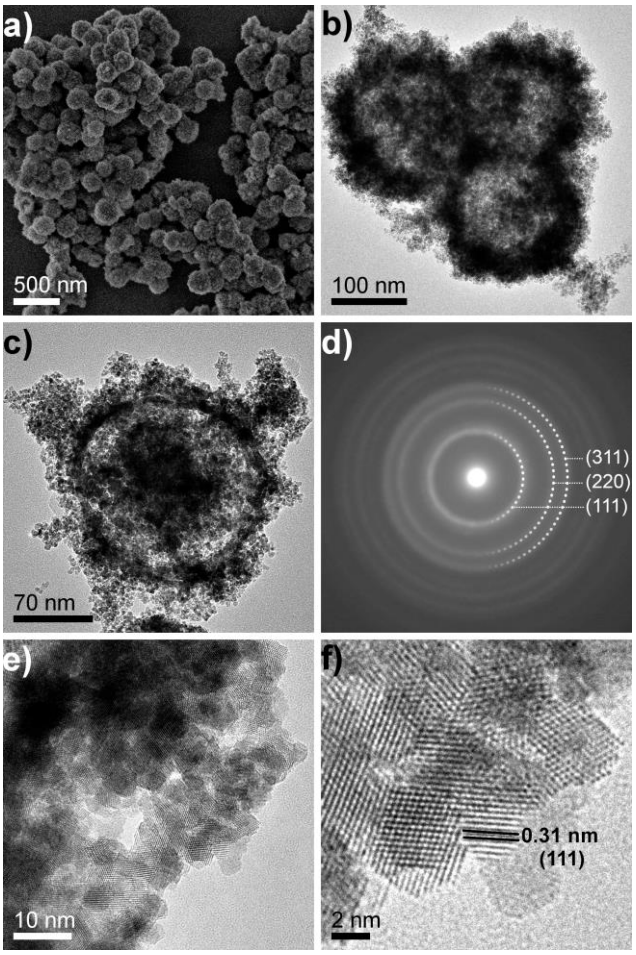

Figure 2. (a) FESEM image (b) TEM image, (c) TEM image showing a single nanosphere, (d) SAED pattern, and (e,f) HRTEM images of yolk-shell CeO_2 nanospheres.

To obtain a deeper understanding of the crystal structure of yolk-shell CeO_2 nanospheres, we perform the PDF analysis. The experimental PDF ($G(r)$) of the sample is fitted in the r range of 1.5 Å < r < 50 Å applying the crystallographic data of cubic CeO_2 (a = 5.4124 Å) from Inorganic Crystal Structure Database [ICSD]: 72155,[36] as shown in Figure 3. For the PDF fit, we refine the unit cell parameter a, scale factor, two anisotropic atomic displacement parameters, one for cerium and one for oxygen, the quadratic atomic correlation factor δ_2, and spherical particle diameter (sp-diameter). Modeling the data against a single phase of CeO_2 results in significant and systematic deviations in the PDF peak intensities. We use two phases of cubic CeO_2 with the same parameters for refinement, except for scale factor and sp-diameter, and obtain good agreement reflected by the weighted residual (R_w) of 0.1139. The refined parameters are given in Table S1. The sp-diameter parameters refine to 82 Å (fraction of 64%) and 23 Å (fraction of 36%). Instead of a strictly bimodal size distribution, we interpret the result as indicative of a wider size distribution of coherent domains within a span of approx. 10–100 Å. Moreover, the predicted (Table S2) and measured (Figure S7) unit cell parameters and the atom pair distances for the first

coordination shells in the fluorite structure are consistent, ruling out the presence of oxygen vacancies in ambient conditions.

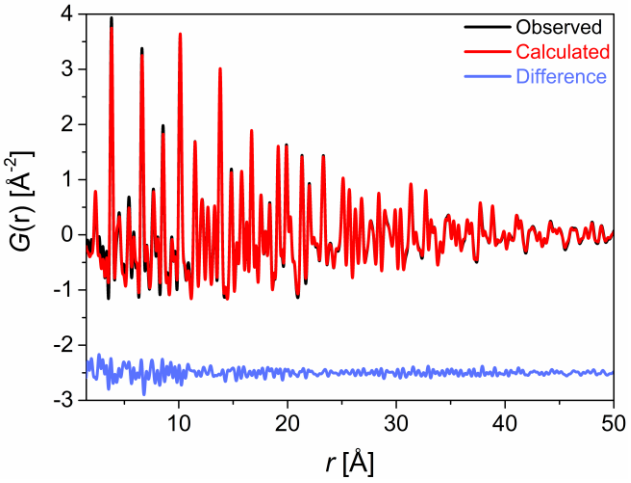

Figure 3. Fit between experimental and calculated $G(r)$ using two identical phases of cubic CeO_2 structure with different sp-diameter and scale factor parameters.

We evaluate the CO_2 sensing performance of yolk-shell CeO_2 nanospheres by monitoring the change in the resistance upon exposure to CO_2 pulses from 150 to 2400 ppm. First, we assess the CO_2 sensing performance at room temperature and 30% RH as shown in Figure S8. At such conditions, the sensor already presents great sensitivity to CO_2; however, the resistance does not completely return to the initial R_0 value between the CO_2 pulses. Thus, to overcome this drawback, we study the CO_2 sensing performance of the yolk-shell ceria nanospheres applying heat. The resistance changes at 70% RH in the temperature range of 100–250 °C (Figure S9) confirm that even the mild heating at 100 °C is enough to achieve the reversibility of the sensor. Figure 4a presents the sensor signals for all CO_2 concentration at 70% RH as a function of the operating temperature. Notably, the sensor signals reach the highest values at 100 °C and decrease with increasing the operating temperature for the whole CO_2 concentration range. The signal to 2400 ppm CO_2 at 100 °C is almost two times higher than those at higher temperatures. The great sensitivity at the low operating temperature of 100 °C seems promising for real applications because so far the best CO_2 sensors exhibit the highest CO_2 sensor signal at temperatures above 200 °C.[11,14] To illustrate the advantages of our sensor, Table S3 presents a summary of the CO_2 sensing performance of different chemoresistive sensors.

To study the effect of humidity on the yolk-shell CeO_2 nanospheres-based sensor, we carry out the CO_2 sensing experiments at 100 °C changing the humidity from 30 to 70% RH as shown in Figure 4b. The electrical resistance of the sensor decreases with increasing the

humidity level, which is explained either due to the electron donation from adsorbed water to the semiconductor,[37] or the interaction of water with ionosorbed oxygen species that releases electrons to the semiconductor.[38] Although the resistance of the sensor decreases with increasing the RH, the quality of the measurement remains unaffected in terms of baseline stability, ability to reach a stable response and recovery to the initial resistance after each CO_2 pulse. Moreover, the increase of RH does not significantly change the response and recovery times, which is advantageous but unusual behavior for chemoresistive sensors.[39] The values of the response and recovery times for each CO_2 concentration are summarized in Table S4. Figure 4c shows the sensor signal at 100 °C versus CO_2 concentration and indicates an enhancement in the signal as increasing RH from 30 to 70%. These observations suggest the positive influence of humidity on the CO_2 sensing performance of yolk-shell CeO_2 nanospheres. The curves of the logarithm of the sensor signal *versus* the logarithm of the CO_2 concentration at 30–70% RH are presented in Figure S10 and exhibit great linear fitting.

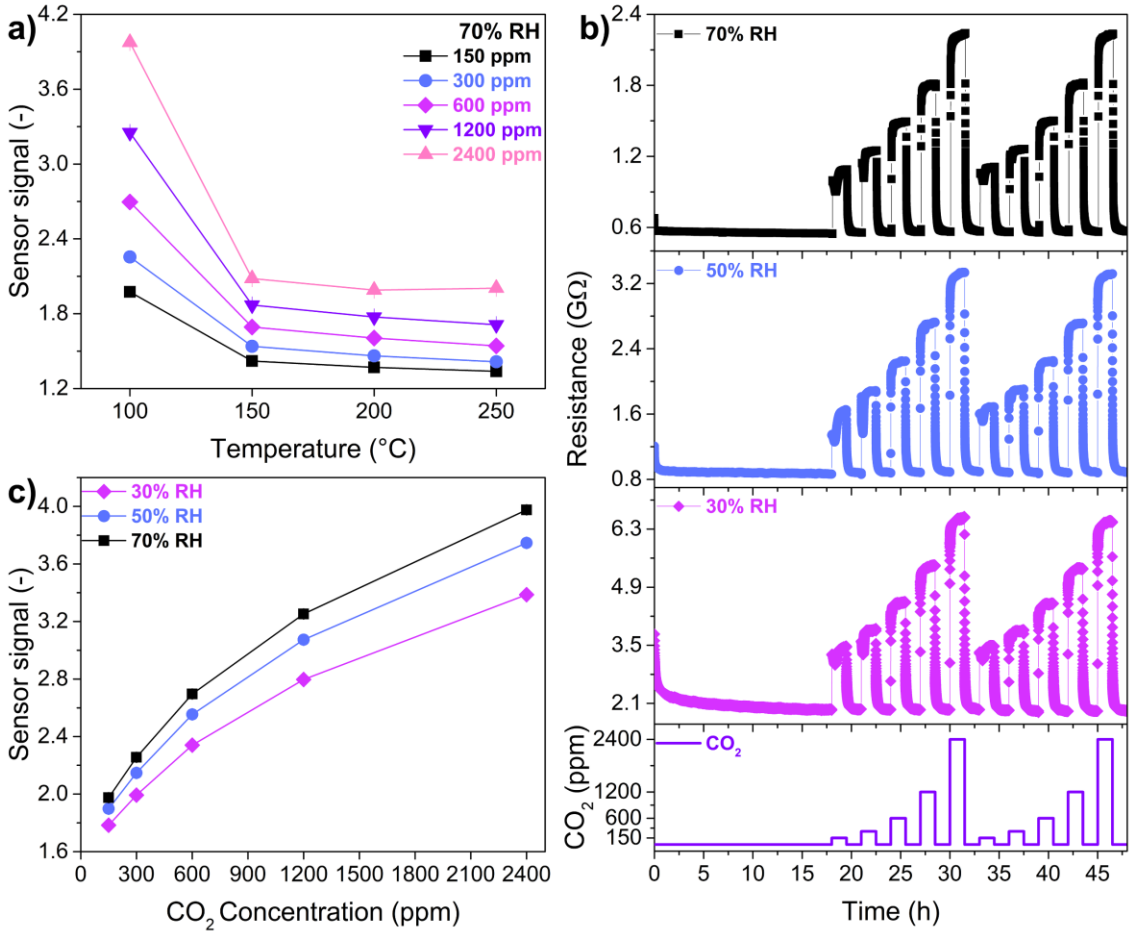

Figure 4. CO_2 sensing performance of yolk-shell CeO_2 nanospheres. (a) Sensor signal to the CO_2 concentration range of 150-2400 ppm as a function of the operating temperature at 70% RH. (b) Resistance changes of the sensor during CO_2 pulses in the concentration range of 150-2400 ppm in humid air (at 30, 50, and 70% RH). (c) Sensor signal as a function of CO_2 concentration at 30–70% RH at 100 °C.

To investigate the role of the yolk-shell structure on the CO_2 sensing performance, we compare the sensing properties of the yolk-shell CeO_2 nanospheres with those of commercial CeO_2 powder (FESEM images shown in Figure S11) at 100 °C and 70% RH, as displayed in Figure 5. The response curves for both sensors evidence the distinct behavior between them; on the one hand, the yolk-shell CeO_2 nanospheres show improved baseline stability and reversibility, on the other hand, commercial CeO_2 nanoparticles present long response times, a drift of the baseline resistance, and a poor reversibility after the CO_2 pulses, i.e., the resistance does not fully recover to the initial value as shown in Figure 5a. At the highest CO_2 concentration of 2400 ppm, yolk-shell CeO_2 nanospheres present an almost 20-fold faster response time than commercial CeO_2 nanoparticles (Figure 5b,c) and a recovery time of 4.08 min, which is better than the irreversibility of the commercial powder. Furthermore, the yolk-shell CeO_2 nanospheres have superior sensitivity: the sensor signals reach values 1.8–2.9 times higher than those for commercial CeO_2 nanoparticles, as shown in Figure 5d.

We hypothesize that the higher stability, faster response and recovery times, and reversibility of yolk-shell nanospheres are due to their unique hollow and porous structure. This kind of structure allows for effective and rapid gas diffusion through the whole material even into the inner part of the nanospheres. Not only the analyte gas effectively diffuses toward the sensing film, but also the carrier gas, enhancing the recovery of the sensor after CO_2 pulses. On the other hand, commercial ceria nanoparticles are bigger, denser, and impermeable, which result in poor gas diffusion in the sensing film.[40] Consequently, commercial CeO_2 presents long response times and ineffective desorption of CO_2 species from the surface as suggested by the irreversibility of the sensor. This partial recovery also promotes a significant drift in the baseline resistance between the CO_2 pulses, which we propose to be attributed to the remaining adsorbed species on the surface.[41,42]

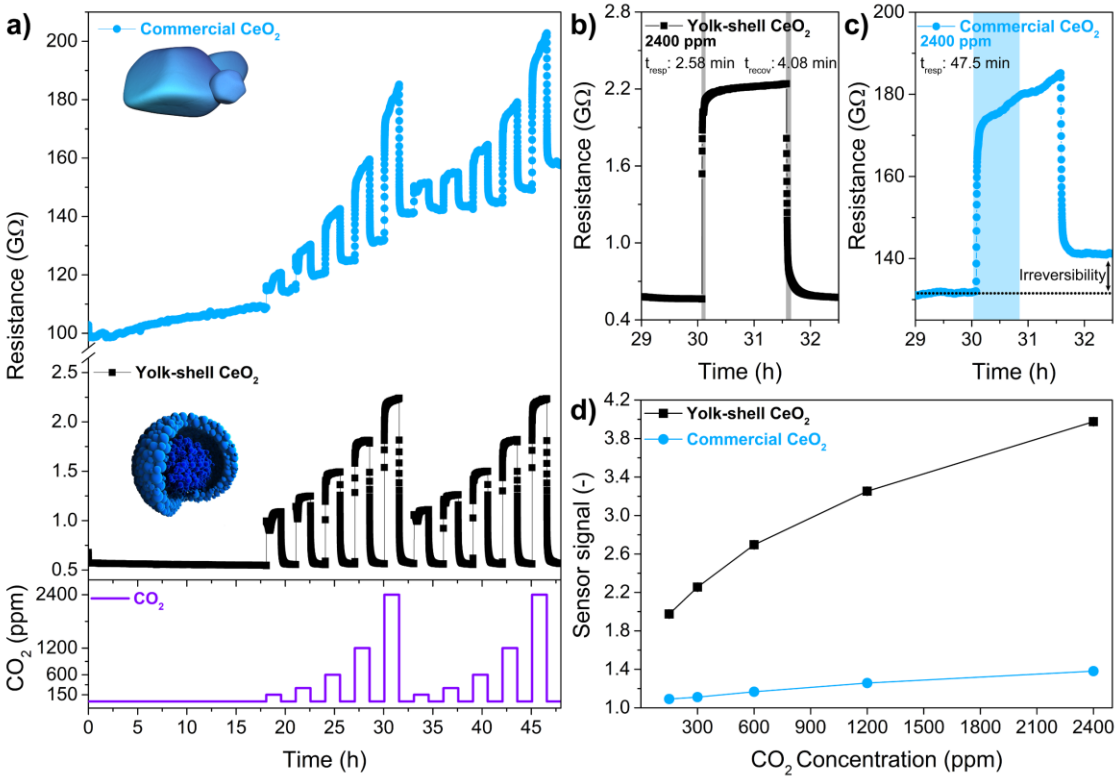

Figure 5. Comparison of the CO_2 sensing performance of yolk-shell CeO_2 nanospheres and commercial CeO_2 nanoparticles at 70% RH and 100 °C. (a) Resistance changes of the sensors upon CO_2 exposures in the concentration range of 150-2400 ppm. (b) Response and recovery times to 2400 ppm of the yolk-shell CeO_2-based sensor. (c) Response time to 2400 ppm of commercial CeO_2 nanoparticles. (d) Sensor signal of the sensors as a function of CO_2 concentration.

To test this hypothesis and understand the clear differences seen in the CO_2-sensing performance between yolk-shell CeO_2 nanospheres and commercial CeO_2 nanoparticles, we evaluate their respective specific surface areas and CO_2 adsorption capacities. The BET specific surface area of yolk-shell CeO_2 nanospheres is 85 m^2 g^{-1}, which is sixteen times higher than that of commercial CeO_2 powder (5.4 m^2 g^{-1}). At 100 °C the weight gain after CO_2 exposure reveals a stronger interaction of CO_2 with the yolk-shell CeO_2 nanospheres than with the commercial CeO_2 powder as shown in TG curve in Figure 6. The yolk-shell CeO_2 nanospheres can adsorb 10.36 mg of CO_2 per 1g of the sample, whereas the commercial CeO_2 powder only adsorbs 4.73 mg g^{-1}. The improved CO_2 adsorption capacity can be due to the higher surface area and porosity of the yolk-shell nanospheres that enhances the gas diffusion inside the nanoparticles. Thus, supporting our hypothesis that the enhanced sensing performance of the yolk-shell nanospheres is related directly to the morphology of the sensing film.

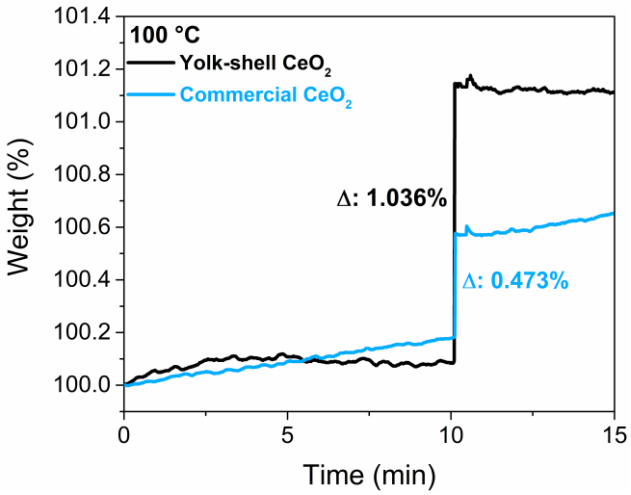

Figure 6. TG curves of adsorption of CO_2 on yolk-shell CeO_2 nanospheres and commercial CeO_2 nanoparticles at 100 °C.

This is also in line with previous in situ X-ray spectroscopic synchrotron studies on rare-earth materials. For example, it was shown that CeO_2 and $La_2O_2CO_3$ are not reduced under H_2O_2 or CO_2 exposure at low temperatures, but instead, they act as an "electron sponges". A possible explanation of the CO_2 sensitivity is the formation of metal carbonate-related species on the surface, which changes the density of states at rare-earth metal and results in changes of the resistance of the sensor. The TG analysis revealed that the yolk-shell morphology of our ceria nanospheres gives rise to higher number of active sites at the surface for CO_2 adsorption, which likely result in a greater probability of forming carbonate-related species. Indeed, we observe various carbonate stretching vibrations of CO_3^{2-} in the IR spectra of yolk-shell sample as shown in Supporting Information, Figure S4. However, the type of carbonate species changing upon exposure to CO_2 can be only determined in further in situ mechanistic studies, which exceeds the scope of the contribution.

4. Conclusions

In summary, we present a simple strategy to fabricate a high-performance chemoresistive CO_2 sensor based on yolk-shell CeO_2 nanospheres that operates at temperature of 100 °C in humid air. We show that the yolk-shell CeO_2 nanospheres-based sensor is much more sensitive to CO_2, stable, reversible, and faster than the sensor based on commercial CeO_2 nanoparticles. Moreover, our CO_2 adsorption measurement evidences the high adsorption capacity of yolk-shell nanospheres compared with the commercial nanoparticles. Thus, the design hollow nanostructured metal oxides with a high specific surface area and porous shells can be an efficient alternative to develop sensitive CO_2 sensors for practical applications. To meet the requirements of a real sensor, nonetheless, further improvements are needed. The response

and recovery times of the yolk-shell CeO_2 nanospheres-based sensor are in the order of minutes. Therefore, in addition to the inherent porosity of an individual nanosphere that allows for gas diffusion, the increase and acceleration of gas diffusion through the whole sensitive film can be used to overcome such drawbacks. For instance, inkjet-printing of the metal oxide can be explored to produce hierarchical porous film and reach even faster response and recovery times.[43]

Acknowledgments

We thank the São Paulo Research Foundation (FAPESP; grants 2018/08271-7, 2016/25267-8, 2016/00033-0, 2017/01267-1, 2018/01258-5), National Council for Scientific and Technological Development (CNPs, grant 308327/2018-7), and the financial support by the Federal Ministry of Education and Research of Germany (BMBF) in the framework of LUCENT (project number 05K19GU7). We acknowledge the LMA/IQ/UNESP and LMEOQ/IQ/UNICAMP for the FESEM and Raman facilities, respectively and the Brazilian Nanotechnology National Laboratory – LNNano/CNPEM (proposals n. 23272 and 24307) for the XPS and TEM facilities. Parts of this research were carried out at P07 beamline at PETRA III at DESY (Hamburg, Germany), a member of the Helmholtz Association HGF, and we would like to thank the beamline staff for the assistance in the experiments.

References

(1) Ritchie, H.; Roser, M. CO_2 and Other Greenhouse Gas Emissions. *OurWorldInData.org* **2015**. https://doi.org/10.1034/j.1399-0004.2002.610606.x.

(2) Permentier, K.; Vercammen, S.; Soetaert, S.; Schellemans, C. Carbon Dioxide Poisoning: A Literature Review of an Often Forgotten Cause of Intoxication in the Emergency Department. *Int. J. Emerg. Med.* **2017**, *10* (1), 14. https://doi.org/10.1186/s12245-017-0142-y.

(3) Firl, C.; Argudin, R. New OSHA Rescue Requirements for Confined Space Retrieval: What You Should Know. *Occup. Health Saf.* **2015**.

(4) Moumen, S.; Raible, I.; Krauß, A.; Wöllenstein, J. Infrared Investigation of CO_2 Sorption by Amine Based Materials for the Development of a NDIR CO_2 Sensor. *Sensors Actuators B Chem.* **2016**, *236*, 1083–1090. https://doi.org/10.1016/j.snb.2016.06.014.

(5) Kim, T.-W.; Kim, J.-W.; Lee, S.-M.; Park, C.-O. Humidity Effects on the Initial

Stabilization Behavior of a Solid Electrochemical CO_2 Sensor. *Sensors Actuators B Chem.* **2019**, *295*, 65–69. https://doi.org/10.1016/j.snb.2019.05.015.

(6) Gassensmith, J. J.; Kim, J. Y.; Holcroft, J. M.; Farha, O. K.; Stoddart, J. F.; Hupp, J. T.; Jeong, N. C. A Metal–Organic Framework-Based Material for Electrochemical Sensing of Carbon Dioxide. *J. Am. Chem. Soc.* **2014**, *136* (23), 8277–8282. https://doi.org/10.1021/ja5006465.

(7) Shang, J.; Lin, S.; Theato, P. Fabrication of Color Changeable CO_2 Sensitive Nanofibers. *Polym. Chem.* **2017**, *8* (48), 7446–7451. https://doi.org/10.1039/C7PY01628J.

(8) Korotcenkov, G. *Handbook of Gas Sensor Materials*; Integrated Analytical Systems; Springer New York: New York, NY, 2013. https://doi.org/10.1007/978-1-4614-7165-3.

(9) Wang, D.; Chen, Y.; Liu, Z.; Li, L.; Shi, C.; Qin, H.; Hu, J. CO_2-Sensing Properties and Mechanism of Nano-SnO_2 Thick-Film Sensor. *Sensors Actuators B Chem.* **2016**, *227*, 73–84. https://doi.org/10.1016/j.snb.2015.12.025.

(10) Hirsch, O.; Kvashnina, K. O.; Luo, L.; Süess, M. J.; Glatzel, P.; Koziej, D. High-Energy Resolution X-Ray Absorption and Emission Spectroscopy Reveals Insight into Unique Selectivity of La-Based Nanoparticles for CO_2. *Proc. Natl. Acad. Sci.* **2015**, *112* (52), 15803–15808. https://doi.org/10.1073/pnas.1516192113.

(11) Djerdj, I.; Haensch, A.; Koziej, D.; Pokhrel, S.; Barsan, N.; Weimar, U.; Niederberger, M. Neodymium Dioxide Carbonate as a Sensing Layer for Chemoresistive CO_2 Sensing. *Chem. Mater.* **2009**, *21* (22), 5375–5381. https://doi.org/10.1021/cm9013392.

(12) Tanvir, N. B.; Yurchenko, O.; Laubender, E.; Pohle, R.; Sicard, O. v.; Urban, G. Zinc Peroxide Combustion Promoter in Preparation of CuO Layers for Conductometric CO_2 Sensing. *Sensors Actuators B Chem.* **2018**, *257*, 1027–1034. https://doi.org/10.1016/j.snb.2017.11.055.

(13) Kanaparthi, S.; Singh, S. G. Chemiresistive Sensor Based on Zinc Oxide Nanoflakes for CO_2 Detection. *ACS Appl. Nano Mater.* **2019**, *2* (2), 700–706. https://doi.org/10.1021/acsanm.8b01763.

(14) Chapelle, A.; El Younsi, I.; Vitale, S.; Thimont, Y.; Nelis, T.; Presmanes, L.; Barnabé, A.; Tailhades, P. Improved Semiconducting CuO/$CuFe_2O_4$ Nanostructured Thin Films for CO_2 Gas Sensing. *Sensors Actuators B Chem.* **2014**, *204*, 407–413.

https://doi.org/10.1016/j.snb.2014.07.088.

(15) Joshi, S.; C. B., R. K.; Jones, L. A.; Mayes, E. L. H.; Ippolito, S. J.; Sunkara, M. V. Modulating Interleaved ZnO Assembly with CuO Nanoleaves for Multifunctional Performance: Perdurable CO_2 Gas Sensor and Visible Light Catalyst. *Inorg. Chem. Front.* **2017**, *4* (11), 1848–1861. https://doi.org/10.1039/C7QI00474E.

(16) Joshi, S.; Ippolito, S. J.; Periasamy, S.; Sabri, Y. M.; Sunkara, M. V. Efficient Heterostructures of Ag@CuO/$BaTiO_3$ for Low-Temperature CO_2 Gas Detection: Assessing the Role of Nanointerfaces during Sensing by Operando DRIFTS Technique. *ACS Appl. Mater. Interfaces* **2017**, *9* (32), 27014–27026. https://doi.org/10.1021/acsami.7b07051.

(17) Holzinger, M. Potentiometric Detection of Complex Gases: Application to CO_2. *Solid State Ionics* **1997**, *94* (1–4), 217–225. https://doi.org/10.1016/S0167-2738(96)00583-8.

(18) Chen, G.; Han, B.; Deng, S.; Wang, Y.; Wang, Y. Lanthanum Dioxide Carbonate $La_2O_2CO_3$ Nanorods as a Sensing Material for Chemoresistive CO_2 Gas Sensor. *Electrochim. Acta* **2014**, *127*, 355–361. https://doi.org/10.1016/j.electacta.2014.02.075.

(19) Willa, C.; Yuan, J.; Niederberger, M.; Koziej, D. When Nanoparticles Meet Poly(Ionic Liquid)s: Chemoresistive CO_2 Sensing at Room Temperature. *Adv. Funct. Mater.* **2015**, *25* (17), 2537–2542. https://doi.org/10.1002/adfm.201500314.

(20) Willa, C.; Schmid, A.; Briand, D.; Yuan, J.; Koziej, D. Lightweight, Room-Temperature CO_2 Gas Sensor Based on Rare-Earth Metal-Free Composites—An Impedance Study. *ACS Appl. Mater. Interfaces* **2017**, *9* (30), 25553–25558. https://doi.org/10.1021/acsami.7b07379.

(21) Rebber, M.; Willa, C.; Koziej, D. Organic–Inorganic Hybrids for CO_2 Sensing, Separation and Conversion. *Nanoscale Horizons* **2020**. https://doi.org/10.1039/C9NH00380K.

(22) Gyger, F.; Hübner, M.; Feldmann, C.; Barsan, N.; Weimar, U. Nanoscale SnO_2 Hollow Spheres and Their Application as a Gas-Sensing Material. *Chem. Mater.* **2010**, *22* (16), 4821–4827. https://doi.org/10.1021/cm1011235.

(23) Bulemo, P. M.; Cho, H.-J.; Kim, D.-H.; Kim, I.-D. Facile Synthesis of Pt-Functionalized Meso/Macroporous SnO_2 Hollow Spheres through in Situ Templating with SiO_2 for H_2S Sensors. *ACS Appl. Mater. Interfaces* **2018**, *10* (21), 18183–18191.

https://doi.org/10.1021/acsami.8b00901.

(24) Hu, J.; Sun, Y.; Xue, Y.; Zhang, M.; Li, P.; Lian, K.; Zhuiykov, S.; Zhang, W.; Chen, Y. Highly Sensitive and Ultra-Fast Gas Sensor Based on CeO_2-Loaded In_2O_3 Hollow Spheres for Ppb-Level Hydrogen Detection. *Sensors Actuators B Chem.* **2018**, *257*, 124–135. https://doi.org/10.1016/j.snb.2017.10.139.

(25) Wang, L.; Lou, Z.; Deng, J.; Zhang, R.; Zhang, T. Ethanol Gas Detection Using a Yolk-Shell (Core-Shell) α-Fe_2O_3 Nanospheres as Sensing Material. *ACS Appl. Mater. Interfaces* **2015**, *7* (23), 13098–13104. https://doi.org/10.1021/acsami.5b03978.

(26) Zou, Y.; Chen, S.; Sun, J.; Liu, J.; Che, Y.; Liu, X.; Zhang, J.; Yang, D. Highly Efficient Gas Sensor Using a Hollow SnO_2 Microfiber for Triethylamine Detection. *ACS Sensors* **2017**, *2* (7), 897–902. https://doi.org/10.1021/acssensors.7b00276.

(27) Zhang, R.; Zhang, T.; Zhou, T.; Lou, Z.; Deng, J.; Wang, L. Fast and Real-Time Acetone Gas Sensor Using Hybrid $ZnFe_2O_4$/ZnO Hollow Spheres. *RSC Adv.* **2016**, *6* (71), 66738–66744. https://doi.org/10.1039/C6RA12201A.

(28) Li, X.; Zhou, X.; Guo, H.; Wang, C.; Liu, J.; Sun, P.; Liu, F.; Lu, G. Design of Au@ZnO Yolk–Shell Nanospheres with Enhanced Gas Sensing Properties. *ACS Appl. Mater. Interfaces* **2014**, *6* (21), 18661–18667. https://doi.org/10.1021/am5057322.

(29) Xie, A.; Guo, J.; Liu, W.; Yang, Y. Template-Free Synthesis of Core–Shell CeO_2 Nanospheres. *RSC Adv.* **2014**, *4* (22), 11357. https://doi.org/10.1039/c3ra46292g.

(30) Elson Longo da Silva; José Arana Varela; David Keyson de Araújo Almeida; Diogo Paschoalini Volanti. Microwave Aided Device for Hydrothermal Synthesis of Nanostructured Oxides, Particularly Obtaining Particles of Metal Oxides, Comprises Container, in Which Hydrothermal Reaction Takes Place, and Lid for Container. BR200815393-A2, 2010.

(31) Ashiotis, G.; Deschildre, A.; Nawaz, Z.; Wright, J. P.; Karkoulis, D.; Picca, F. E.; Kieffer, J. The Fast Azimuthal Integration Python Library: PyFAI. *J. Appl. Crystallogr.* **2015**, *48*, 510–519. https://doi.org/10.1107/S1600576715004306.

(32) Juhás, P.; Davis, T.; Farrow, C. L.; Billinge, S. J. L. PDFgetX3: A Rapid and Highly Automatable Program for Processing Powder Diffraction Data into Total Scattering Pair Distribution Functions. *J. Appl. Crystallogr.* **2013**, *46* (2), 560–566. https://doi.org/10.1107/S0021889813005190.

(33) Farrow, C. L.; Juhas, P.; Liu, J. W.; Bryndin, D.; Božin, E. S.; Bloch, J.; Proffen, T.; Billinge, S. J. L. PDFfit2 and PDFgui: Computer Programs for Studying Nanostructure in Crystals. *J. Phys. Condens. Matter* **2007**, *19* (33), 335219. https://doi.org/10.1088/0953-8984/19/33/335219.

(34) Plaza, M. G.; Pevida, C.; Arias, B.; Fermoso, J.; Arenillas, A.; Rubiera, F.; Pis, J. J. Application of Thermogravimetric Analysis to the Evaluation of Aminated Solid Sorbents for CO_2 Capture. *J. Therm. Anal. Calorim.* **2008**, *92* (2), 601–606. https://doi.org/10.1007/s10973-007-8493-x.

(35) Ojwang, D. O.; Grins, J.; Svensson, G. The Adsorption Kinetics of CO_2 on Copper Hexacyanoferrate Studied by Thermogravimetric Analysis. *Microporous Mesoporous Mater.* **2018**, *272*, 70–78. https://doi.org/10.1016/j.micromeso.2018.06.019.

(36) WoŁcyrz, M.; Kepinski, L. Rietveld Refinement of the Structure of CeOCI Formed in Pd/CeO_2 Catalyst: Notes on the Existence of a Stabilized Tetragonal Phase of La_2O_3 in LaPdO System. *J. Solid State Chem.* **1992**, *99* (2), 409–413. https://doi.org/10.1016/0022-4596(92)90330-X.

(37) Boyle, J. F.; Jones, K. A. The Effects of CO, Water Vapor and Surface Temperature on the Conductivity of a SnO_2 Gas Sensor. *J. Electron. Mater.* **1977**, *6* (6), 717–733. https://doi.org/10.1007/BF02660346.

(38) Chen, Z.; Lu, C. Humidity Sensors: A Review of Materials and Mechanisms. *Sens. Lett.* **2005**, *3* (4), 274–295. https://doi.org/10.1166/sl.2005.045.

(39) Tian, H.; Fan, H.; Li, M.; Ma, L. Zeolitic Imidazolate Framework Coated ZnO Nanorods as Molecular Sieving to Improve Selectivity of Formaldehyde Gas Sensor. *ACS Sensors* **2016**, *1* (3), 243–250. https://doi.org/10.1021/acssensors.5b00236.

(40) Lee, J.-H. Gas Sensors Using Hierarchical and Hollow Oxide Nanostructures: Overview. *Sensors Actuators B Chem.* **2009**, *140* (1), 319–336. https://doi.org/10.1016/j.snb.2009.04.026.

(41) Fennell, J. F.; Liu, S. F.; Azzarelli, J. M.; Weis, J. G.; Rochat, S.; Mirica, K. A.; Ravnsbaek, J. B.; Swager, T. M. Nanowire Chemical/Biological Sensors: Status and a Roadmap for the Future. *Angew. Chem. Int. Ed. Engl.* **2016**, *55* (4), 1266–1281. https://doi.org/10.1002/anie.201505308.

(42) Korotcenkov, G.; Cho, B. K. Instability of Metal Oxide-Based Conductometric Gas

Sensors and Approaches to Stability Improvement (Short Survey). *Sensors Actuators B Chem.* **2011**, *156* (2), 527–538. https://doi.org/10.1016/j.snb.2011.02.024.

(43) Von Hagen, R.; Sneha, M.; Mathur, S. Ink-Jet Printing of Hollow SnO_2 Nanospheres for Gas Sensing Applications. *J. Am. Ceram. Soc.* **2014**, *97* (4), 1035–1040. https://doi.org/10.1111/jace.12832.